

# Synthesis of Flexible Phase Change Materials with In Situ Formed Porous TiO<sub>2</sub> for Highly Efficient Battery Thermal Management

Guangyuan Liang, Runyang Wang, Qiang Zhou, Jiahuan He, Yuanzheng Liu, Jiateng Zhao, and Changhui Liu\*

To address the dual challenges of fragile structures prone to damage and packaging systems susceptible to leakage in thermal management of electronic devices for traditional phase change materials, this study proposes an organic-porous synergistic packaging strategy. A porous TiO<sub>2</sub> skeleton is in situ constructed via a one-pot one-step method to synchronously encapsulate paraffin wax and thermoplastic elastomer styrene ethylene butylene styrene (SEBS). The innovation lies in utilizing solvent evaporation-induced phase separation and sol-gel reaction to enable the

porous TiO<sub>2</sub> (specific surface area 316.307 m<sup>2</sup> g<sup>-1</sup>) and SEBS to form a rigid-flexible synergistic structure, achieving low leakage rate and stability in 2000 thermal cycles. In battery thermal management, the battery temperature is controlled within a safe range at 1–3C rates, extending the safe operation duration of the battery by more than 10 times. It provides a referable option for efficient thermal management of wearable electronic devices and flexible devices.

## 1. Introduction

With the rapid advancement of modern technology, the miniaturization and high-power density of electronic devices have rendered heat dissipation an increasingly prominent challenge, emerging as a critical bottleneck that restricts their performance, reliability, safety, and service life. The substantial thermal energy generated during operation not only accelerates component aging and induces performance degradation but also poses risks of safety accidents such as thermal runaway. Consequently, efficient and reliable thermal management technologies have become indispensable.<sup>[1–5]</sup> Battery thermal management (BTM) technologies mainly include air cooling, liquid cooling, and phase change materials (PCMs) cooling. Air cooling, the earliest developed and simplest thermal management method, remains the most mature. However, due to the low thermal conductivity and heat transfer efficiency of air, it is difficult to maintain appropriate operating temperatures and temperature uniformity under complex working conditions.<sup>[6]</sup> The heat transfer coefficient of liquid cooling is significantly higher than that of air, offering better thermal management effects. However, its intricate structure imposes stringent requirements for installation and maintenance, and furthermore necessitates the inclusion of auxiliary components such as pumps.<sup>[7,8]</sup> PCMs have gradually assumed a pivotal role in BTM, leveraging advantages including low-cost, high-energy density, excellent long-term cyclic performance, and

constant working temperature.<sup>[9–11]</sup> They efficiently absorb pulsed heat and mitigate temperature fluctuations, with the energy storage process consuming no additional power, thus making up for the shortcomings of traditional thermal management technology such as high energy consumption and limited heat storage capacity.<sup>[12–15]</sup>

PCMs promotes the redistribution of heat within battery modules by establishing isothermal phase change interfaces. In composite PCMs systems, high thermal conductivity fillers form rapid heat conduction paths to reduce temperature differences between batteries. For example, Gao et al.<sup>[11]</sup> used hyperbolic graphene aerogels as thermal conductive skeletons, achieving a high thermal conductivity of 30.75 W/(m K) at low loading, and stabilizing the battery temperature below 42 °C at a 3.75C rate; Dai et al.<sup>[16]</sup> prepared a microencapsulated inorganic hydrated salt phase change composite system, effectively improving the heat storage performance and thermal stability of inorganic PCMs. At a high discharge rate of 2C, the peak temperature of the battery module decreased from 76 °C to 61.2 °C, with the temperature difference within the module controlled below 3 °C; Lin et al.<sup>[17]</sup> introduced CNT@MXene aerogel composite PCMs into the BTM system. Their strong electronegativity endows excellent structural and thermal stability, while the 3D network significantly enhances the system's thermal conductivity. This material delays battery aging through efficient thermal regulation, providing an innovative solution for extending the service life of battery packs in electric vehicles and hybrid electric vehicles. Currently, the application of PCMs in the field of BTM faces dual technical bottlenecks: firstly, PCMs composites based on high thermal conductivity fillers have inherent brittleness and insufficient flexibility, making them prone to structural damage under dynamic conditions such as battery pack vibration and extrusion, thus leading to

G. Liang, R. Wang, Q. Zhou, J. He, Y. Liu, J. Zhao, C. Liu  
School of Low-carbon Energy and Power Engineering  
China University of Mining and Technology  
Xuzhou 221116, China  
E-mail: liuch915@cumt.edu.cn

the failure of the thermal conduction network; secondly, inorganic hydrated salt PCMs have thermodynamic stability defects in their encapsulation systems, posing a risk of phase change medium leakage in high-temperature service environments or during long-term cycling, which severely restricts the safety and thermal management efficiency of battery modules. Notably, in recent years, the academic community has carried out systematic explorations around the above core challenges. Through material interface regulation, composite structure design, and micro-nano preparation technology innovation, significant breakthroughs have been achieved in PCMs performance optimization.

PCMs are classified into solid–liquid,<sup>[18]</sup> solid–solid,<sup>[19]</sup> and liquid–gas<sup>[20]</sup> types based on phase transition mechanisms. Among these, solid–liquid PCMs have been extensively studied for their superior energy storage capacity (Storing substantial heat in minimal volume).<sup>[21–23]</sup> However, the leakage of molten states severely restricts their practical applications.<sup>[24–26]</sup> Current solutions primarily involve loading solid–liquid PCMs onto matrices via chemical or physical methods to fabricate shape-stable "form-stable" composite PCMs.<sup>[27]</sup> Common techniques include porous medium encapsulation,<sup>[28]</sup> microencapsulation,<sup>[29]</sup> and electrospinning.<sup>[30]</sup> Among them, the preparation of composite energy storage materials via physical mixing of PCMs with polymeric or porous matrices to maintain stable form during the phase transition process represents the most widely adopted approach.<sup>[31]</sup> This methodology leverages the structural confinement of matrix materials to address the leakage challenges inherent in pure PCMs, while enabling the integration of thermal energy storage capabilities with mechanical stability. The synergistic combination of PCMs and supporting matrices not only ensures the maintenance of material integrity throughout repeated phase change cycles but also facilitates tunable thermal properties, making it a preferred strategy in the development of high-performance energy storage systems. For instance, Liu et al.<sup>[32]</sup> synthesized siloxy organic–inorganic hybrid polymer encapsulation materials via mild hyper crosslinking, achieving a 600% increase in thermal conductivity, 93.7% photothermal efficiency, and antileakage performance. Wang et al.<sup>[33]</sup> formed a quasisolid structure by entangling ultrahigh molecular weight polyvinyl alcohol with PEG-based PCMs. The phase change enthalpy is 185 J g<sup>-1</sup>, and no leakage occurs at 80 °C for 300 min. Guo et al.<sup>[34]</sup> encapsulated PW in graphene microspheres through emulsion polymerization, which integrates the functions of antileakage, self-sensing (temperature/water droplets), and photothermal conversion.

Although shape-stable PCMs effectively suppress leakage and maintain structural stability, their lack of mechanical properties limit application scenarios.<sup>[35]</sup> To address this, flexible phase change materials (FPCMs) have gained attention as an emerging strategy, with preparation approaches mainly including adsorbing PCMs onto flexible porous materials,<sup>[36]</sup> physically blending with flexible polymers,<sup>[37]</sup> or introducing PCM fragments into flexible polymer backbones via chemical grafting/crosslinking.<sup>[38]</sup> Flexible porous materials have become ideal adsorption matrices due to their low density, large specific surface area, and wide pore

size distribution.<sup>[39]</sup> For example, Tao et al.<sup>[40]</sup> prepared a multi-functional 3D sponge framework wrapped with reduced graphene oxide via cyclic impregnation and *in situ* reduction, further introducing PW matrix through vacuum melt infiltration to obtain a shape-stable flexible composite PCMs. Chen et al.<sup>[41]</sup> fabricated eicosane/single-walled carbon nanotube flexible phase change membranes via ultrasonication, which at 27.1% single-walled carbon nanotube content show a high latent heat of 204.8 J g<sup>-1</sup>, stable performance after 200 thermal cycles. Chemical grafting and crosslinking enable fine-tuning of thermal and mechanical properties by selecting PCMs with different molecular weights and types to adjust molecular structures. Kou et al.<sup>[42]</sup> successfully prepared a solid–solid phase change flexible film via copolymerization of melamine, toluene-2,4-diisocyanate, and polyethylene glycol, featuring 118 J g<sup>-1</sup> phase change enthalpy, 10.7 MPa tensile strength, 8.2% elongation at break, over 1000-cycle stability. Jing et al.<sup>[43]</sup> used peroxide decomposition to induce the formation of C–C bonds, constructing styrene ethylene butylene styrene (SEBS)-OBC double networks for encapsulating PW. The product exhibits an elongation at break of 560%, no leakage after 500 cycles, and a phase change enthalpy of 176 kJ kg<sup>-1</sup>. However, the preparation processes of flexible porous materials and chemical grafting/crosslinking are often complex and costly,<sup>[44,45]</sup> making physical blending of PCMs with flexible polymers the most commonly used method.<sup>[46]</sup> Luo et al.<sup>[47]</sup> prepared a multifunctional composite with a sandwich structure of ethylene-vinyl acetate copolymer/PEG/waterborne polyurethane/carbon nanotubes via film forming and pressing, exhibiting latent heats of 71.45 J g<sup>-1</sup>, tensile strength of 12.96 MPa. Deng et al.<sup>[48]</sup> prepared flexible PW/SEBS/POE/EG PCMs via melt blending. Through the optimization of the SEBS/POE ratio, the flexibility, leak-proof performance, and thermal conductivity of the composite material were synergistically enhanced. Luo et al.<sup>[49]</sup> prepared a FPCM composed of GA, PEG, cMWCNTs, and EVA. It not only has high toughness, but also has a photothermal conversion efficiency of 95.27% and a phase-change latent heat of 71.11 J g<sup>-1</sup>, showing great potential in the fields of energy conversion and health monitoring.

It is noteworthy that while the technology of encapsulating PCMs with porous materials has effectively addressed the leakage issue of liquid PCMs, the inherent rigidity of such encapsulation structures significantly restricts the expansion of their practical application scenarios. To this end, the academic community has conducted extensive research, endeavoring to incorporate flexible polymers into PCMs systems with the expectation of endowing materials with superior elastic deformability and environmental adaptability, thereby broadening their application frontiers.<sup>[50]</sup> Nevertheless, research practices have demonstrated that the introduction of flexible polymers has failed to achieve the anticipated optimization of material performance. On the other hand, flexible polymers provide weaker support for PCMs than rigid porous materials, leading to poor encapsulation: liquid PCMs easily exude during phase transitions, especially at high temperatures or during long-term use, compromising material long-term stability and performance reliability. Therefore, the current PCM field faces a critical research gap: how to overcome the

inherent technical barrier between “rigid packaging that prevents leakage but is brittle” and “flexible packaging that is resilient but prone to leakage.” Although previous studies have attempted to combine rigid fillers with flexible matrices to create so-called “rigid-flexible synergistic” structures,<sup>[47–49]</sup> these methods primarily rely on simple physical blending or stepwise impregnation. In the composite materials prepared using this approach, there is often a distinct interface between the rigid filler and the flexible matrix, resulting in poor compatibility, stress concentration, and structural weak points. This prevents the formation of a truly efficient and synergistic overall network. As a result, the material struggles to achieve an ideal balance between flexibility, encapsulation stability, and thermal storage capacity.

The key to FPCM development lies in balancing flexibility while improving heat storage capacity and encapsulation stability, which requires further optimization. This study employs an organic-porous synergistic encapsulation strategy (OPOS), whose core innovation lies in the simultaneous construction of an inorganic porous  $\text{TiO}_2$  network within a flexible SEBS polymer network via an *in situ* sol-gel method. Specifically, we uniformly mix molten PCM, SEBS dissolved in a solvent, and the  $\text{TiO}_2$  precursor TBT. Subsequently, through the *in situ* hydrolysis of TBT, a highly cross-linked porous  $\text{TiO}_2$  framework is generated within the SEBS elastomer network, intertwined with it. Unlike previous studies on rigid-flexible hybrid structures, the OPOS strategy overcomes the issue of uneven encapsulation caused by surface tension and capillary forces in traditional methods. Through synergistic encapsulation, the flexible SEBS, as a thermoplastic elastomer, provides macroscopic flexibility and mechanical strength, while the *in situ* generated nanoporous  $\text{TiO}_2$  network firmly “locks” PCM molecules in place via strong capillary forces,

preventing PCM leakage, thereby achieving a perfect combination of rigid confinement and flexible support. The resulting PCM exhibits an interface-free structure, as the  $\text{TiO}_2$  network is *in situ* grown within the SEBS matrix, forming an interpenetrating network structure with no distinct interface. This avoids the performance shortcomings of traditional composites caused by interface incompatibility, endowing the material with excellent structural integrity.<sup>[50]</sup> Compared with traditional physical blending or vacuum adsorption, OPOS-prepared materials exhibit higher latent heat ( $116.30 \text{ J g}^{-1}$ ), lower leakage rate, and significantly optimized flexibility (200% increased elongation at break) and mechanical strength (8.7 MPa tensile strength), offering new insights for large-scale applications of PCMs in fields such as wearable electronics and flexible devices.

## 2. Experimental Section

### 2.1. Raw Materials

The SEBS was obtained from Kraton Polymers Company (USA). Paraffin wax (PW) (the melting temperature is about  $32^\circ\text{C}$ ) was provided by Shang Hai Joule Wax Co., Ltd. (China). 1,2-Dichloroethane (DCE) was purchased from National Medicines Corporation Ltd, (China). Tetrabutyl titanate (TBT) was obtained from Macklin chemical Reagent Corp. (Shanghai, China).

### 2.2. Fabrication of FPCM

A one-pot one-step method was used to prepare FPCMs. The specific steps are shown in Figure 1. The reaction was carried out in a

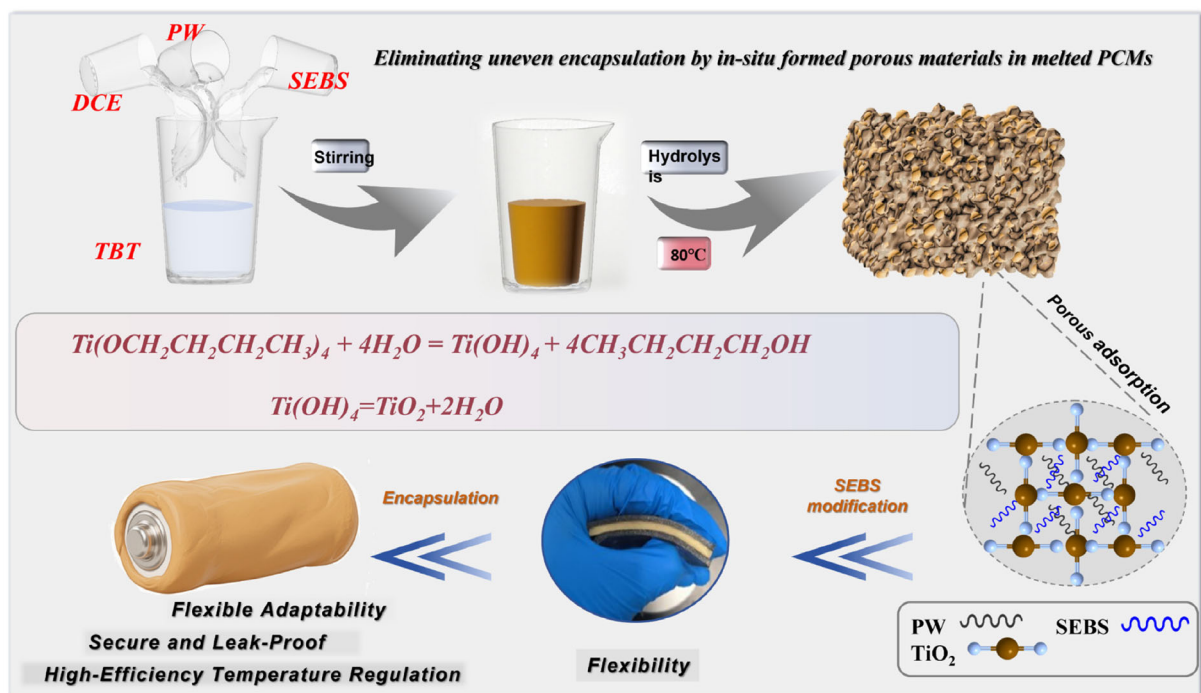


Figure 1. Schematic illustration of the composite fabrication process and principle.

50 ml round-bottom flask. Taking the preparation of SP3 as an example. First, 5.0 g of PW was heated and melted in an oil bath at 80 °C for 30 min to ensure it was completely melted and in a liquid state. Subsequently, 1.0 g of SEBS and 30.0 g of DCE were added to the molten PW. As an organic solvent for SEBS, DCE helped SEBS form a uniform mixed system with PW. The mixture was continuously stirred at 80 °C for 2 h until a uniform SEBS/PW solution was formed. This step ensured that SEBS could be fully dispersed in the PCM, thereby improving the flexibility and stability of the composite material. Next, 3.0 g of TBT was added to the above SEBS/PW solution, and the TBT was fully fused with the mixture by rapid stirring for 30 s to form a uniform mixed system. Then, 0.6 g of deionized water was slowly dropped into the mixture. The water underwent a hydrolysis reaction with TBT to generate solid titanium dioxide at 80 °C.

After completing the above steps, the obtained mixture was placed in a vacuum rotary evaporator, and DCE, butanol, and water were evaporated at 60 °C to obtain a preliminarily solidified composite material. Finally, the obtained solid sample was placed in a vacuum drying oven and further dried under low pressure for 48 h to make the composite material fully solidified and meet the final performance requirements. This method realizes the *in situ* construction of the TiO<sub>2</sub> skeleton and the synchronous encapsulation of the PCM and flexible material through the synergistic effect of solvent evaporation-induced phase separation and sol-gel, avoiding the interfacial compatibility problem in the preparation of the traditional step-by-step method. Materials modified with SEBS possess flexibility and can be used for thermal management in packaged electronic devices. This material features flexible adaptability, safe leakage prevention, and efficient temperature regulation.

As shown in **Table 1**, in order to improve the performance of the composite heat storage material, quantitative PW and TBT were used to study the influence of different SEBS ratios in the composite system. Then, by fixing the mass of PW, the influence of different TBT and SEBS ratios on the performance of the samples in the energy storage system was investigated.

### 2.3. Materials Characterization

The surface or fracture morphology of the sample is observed and analyzed using a scanning electron microscope (SEM, VEGA4). The crystal structure was characterized by D8 ADVANCE X-ray diffractometer (XRD) from Brüker, Germany. The chemical composition of the products was characterized by a Fourier infrared

analyzer (Brüker VERTEX 70 FTIR). The phase change temperature, latent heat of phase change, and thermal cycle stability of the samples are determined by a differential scanning calorimeter (DSC). The measurement of the thermal conductivity of the samples is based on the transient hot-wire method using a Hot Disk 2500-OT thermal conductivity meter manufactured in Sweden. Thermal stability assessments of the samples were conducted through thermogravimetric analysis (TGA) using a TA instruments SDT Q600 analyzer. This analysis was performed in a nitrogen environment, with the temperature escalating from ambient to 800 °C at a uniform rate of 10 °C per minute.

## 3. Results and Discussion

### 3.1. Characterization and Structural Analysis of Resultant Materials

The Fourier transform infrared (FTIR) spectra of the material composition are shown in **Figure 2a**. The peaks of PW at 2960, 2917, and 2849 cm<sup>-1</sup> are attributed to the asymmetric and symmetric stretching vibrations of -CH<sub>2</sub>, respectively; the absorption peaks near 1732, 1471, 1177, and 717 cm<sup>-1</sup> correspond to the rocking vibrations of -CH<sub>2</sub>. The peak of SEBS at 2918 cm<sup>-1</sup> indicates the asymmetric stretching vibration of -CH<sub>2</sub>, while the peaks at 1465 and 698 cm<sup>-1</sup> indicate the rocking vibrations of -CH<sub>3</sub>. According to the FTIR spectral curves of each material, it is clearly observed that no new absorption peaks appear in the prepared PCM samples, and the positions of the absorption peaks do not shift. It is worth noting that except for the characteristic peaks of PW, TiO<sub>2</sub>, and SEBS, no additional peaks are present. This result suggests that during the formation of the composite skeleton, the energy storage activity of the composite remains chemically unchanged regardless of the reaction conditions. Similar observations were obtained through XRD analysis, showing that the main response originates from PW and no crystal changes occur during the preparation process (as shown in **Figure 2b**). The results indicate that the diffraction peaks of the samples are mainly located at  $\theta = 21.6^\circ$  and  $23.8^\circ$ , corresponding to the (110 + 111) and 020 crystal planes of PW, respectively, and no other diffraction peaks appear. Pure PW has the highest diffraction peak intensities at  $\theta = 21.6^\circ$  and  $23.8^\circ$ . As the amount of the flexible material SEBS added increases, the mass of PW in the samples decreases, so the diffraction peak intensities of SP1, SP2, and SP4 gradually decrease. It should be noted that sample information is consistent with our previously reported, thus, some of characterization were identical with our reported data.<sup>[51]</sup>

To observe the micro morphology of the samples, the composite material was tested by SEM. As shown in **Figure 2c**, PW is uniformly encapsulated in the nanotitanium dioxide skeleton generated by the hydrolysis of TBT, proving the formation of a porous nanotitanium dioxide structure. Due to the addition of the flexible polymer SEBS, the amount of PW encapsulated in SP3 is observed to decrease, and the flexible polymer SEBS is also encapsulated in the nanotitanium dioxide skeleton. To clarify the morphological characteristics of the titanium dioxide support

**Table 1.** Study on the different reaction parameters.

Sample	PW/[g]	TBT/[g]	SEBS/[g]	H <sub>2</sub> O/[g]	Reaction temperature/[°C]
PW	5.0	–	–	–	–
SP1	5.0	3.0	–	0.6	90
SP2	5.0	3.0	0.5	0.6	80
SP3	5.0	3.0	1.0	0.6	80
SP4	5.0	3.0	1.5	0.6	80

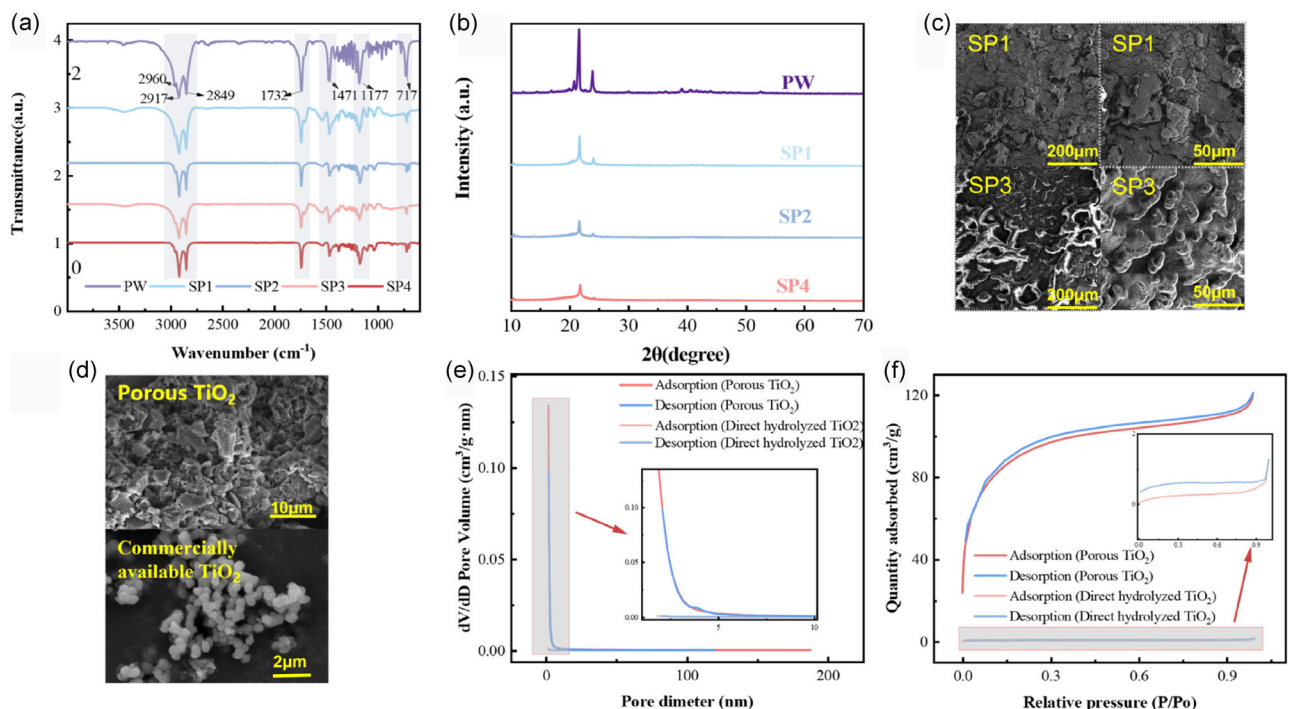


**Figure 2.** Characterization analysis. a) FTIR spectra of PW,  $\text{TiO}_2$ , and composites;<sup>[51]</sup> b) XRD patterns of PW and composites; c) ESM of SP1 and SP3; d) ESM of porous and commercially available  $\text{TiO}_2$ ;<sup>[52]</sup> e) Liquid nitrogen adsorption and desorption curves of porous  $\text{TiO}_2$  and direct hydrolyzed  $\text{TiO}_2$ ; f) Pore size distribution of porous  $\text{TiO}_2$  and direct hydrolyzed  $\text{TiO}_2$ .

structure, petroleum ether and 1,2-dichloroethane were used as solvents to remove the PW and SEBS components in the sample SP3 through ultrasonic-assisted washing, and then the pure titanium dioxide skeleton was obtained by suction filtration separation. As shown in Figure 2d, the treated titanium dioxide exhibits a unique porous network structure, and its morphological characteristics are significantly different from those of commercially available  $\text{TiO}_2$ . This has been reported in our previous work.<sup>[52]</sup>

As can be seen from the SEM images in the above text, the titanium dioxide skeleton prepared in this study has an obvious porous structure, but its internal network porous structure is not clearly displayed. Specific surface area measurement is one of the effective and intuitive methods to reveal the internal porous characteristics. After ultrasonically cleaning the PW in sample SP3 with petroleum ether to ensure its complete removal, the internal solid substance was extracted by suction filtration. Subsequently, it was compared with the titanium dioxide obtained by direct hydrolysis and commercial titanium dioxide, and BET tests were performed on these three titanium dioxide samples. The relevant data are based on the team's previous test conclusions.<sup>[51]</sup>

The test results in **Table 2** show that the specific surface area of the porous titanium dioxide skeleton reaches  $316.307 \text{ m}^2 \text{ g}^{-1}$ , which is much higher than  $0.904 \text{ m}^2 \text{ g}^{-1}$  of the product directly obtained from the reaction of TBT with water and  $0.543 \text{ m}^2 \text{ g}^{-1}$  of commercial  $\text{TiO}_2$ . Its higher specific surface area means an increased contact area with the PCM, thereby generating stronger force after phase transition to achieve better binding effect. Meanwhile, the pore volume of the porous nanotitanium dioxide is also far larger than that of the product from direct hydrolysis

**Table 2.** BET analysis of porous, hydrolyzed, and commercially hydrolyzed  $\text{TiO}_2$ .

Sample	Specific surface area [ $\text{m}^2 \text{ g}^{-1}$ ]	$dV/dD$ pore volume [ $\text{cm}^3 \text{ g}^{-1}$ ]	Average pore diameter [nm]
Porous $\text{TiO}_2$	316.307	0.173292	2.191
Hydrolyzed $\text{TiO}_2$	0.904	0.000890	3.935
Commercially available $\text{TiO}_2$	0.543	0.000125	0.923

and commercial  $\text{TiO}_2$ , and the average pore size distribution of the porous titanium dioxide skeleton is smaller than that of the product from direct hydrolysis, indicating that the prepared porous titanium dioxide has more pores with a pore size below 2 nm. As shown in Figure 2e,f, the isothermal adsorption-desorption curve of the porous titanium dioxide shows that the adsorption capacity under a certain relative pressure is much higher than that of the product from direct hydrolysis. The adsorption-desorption curve exhibits a certain hysteresis phenomenon with a narrow hysteresis loop: the adsorption and desorption branches almost coincide at lower relative pressures but separate at higher relative pressures, indicating that the porous titanium dioxide has a mixed structure of micropores and mesopores. In contrast, the hysteresis loop of the product from direct hydrolysis has no obvious closure point: the desorption branch gradually decreases at lower relative pressures, and the adsorption branch continues to rise at higher relative pressures, indicating that the material has slit pores or nonrigid pore structures formed by the accumulation of flaky particles.

In addition to the microscale pores shown by SEM, the pore size distribution test results also show that the porous titanium dioxide has a large number of nanoscale pores in the 0–5 nm range. This indicates that its skeleton presents a porous network structure, which explains the excellent shape-stabilizing performance of the composite material. It is precisely through the combination of these nanoscale and microscale pores that the shape-stabilizing effect is achieved, and the *in situ* shape stabilization overcomes the problem that the traditional vacuum adsorption method cannot fill the pores at the nanoscale.

### 3.2. Thermal Physical Performance of FPCM Composites

During the long-term use of PCMs, it will undergo multiple phase change cycles, and its cycle stability is crucial for practical applications. Good cycle stability means that the material can maintain phase change temperature, phase change latent heat, and morphological stability during repeated melting-solidification

processes, thereby ensuring its long-term heat storage and release capabilities. SP4 was subjected to 2,000 charging-discharging cycle stability tests. The test steps included heating the sample above the phase change temperature and then placing it in a refrigerator to cool down. After every 100 cycles, part of the sample was taken out for DSC testing. The relevant results are shown in Figure 3a. The performance test results after 2,000 cycles show that the phase change latent heat and phase change temperature of the composite material hardly change, with only slight fluctuations within a certain range. The measurement error within this range is negligible (Figure 3b), so it can be considered that the phase change latent heat of the composite material remains stable. It can be seen that the material maintains high thermal stability, and SP3 exhibits excellent cycle stability and durability.

The thermal stability of the samples was further evaluated by TGA and DTG analysis, as shown in Figure 3c,d, PW starts to pyrolyze at temperatures above 200 °C and is completely pyrolyzed at

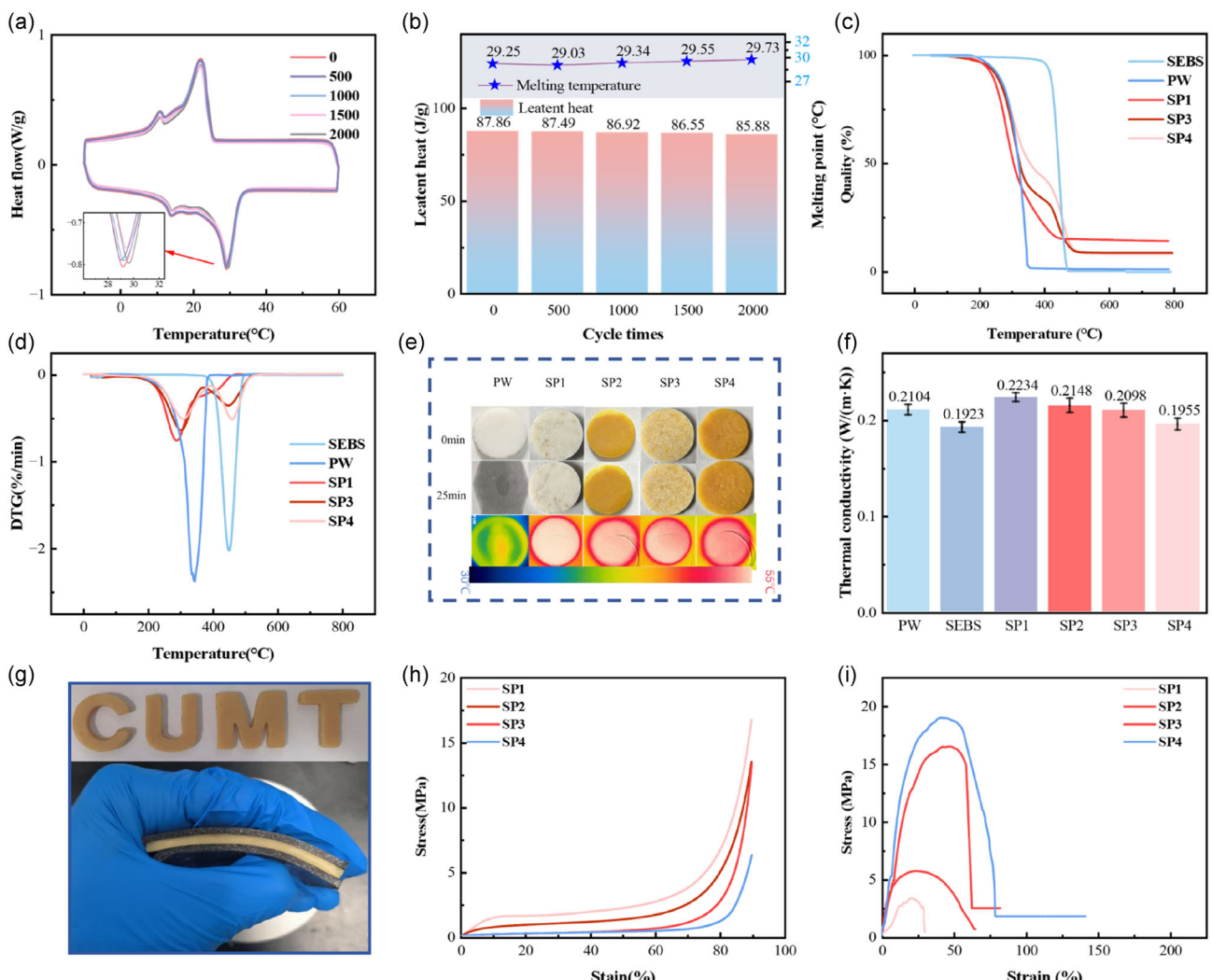


**Figure 3.** Thermal property analysis of the product. a) Cyclic test diagram of SP3I; b) Cyclic stability test diagram of SP3; c) TGA analysis; d) DTG analysis; e) Leakage process visualization of composites; f) Thermal conductivity of PW, SEBS, and composites; g) Sample flexibility display; h) The stress–strain curve of compression performance test; i) The stress–strain curve of tensile performance test.

≈350 °C. The pyrolysis temperature range of SP1 is similar to that of other samples, and the remaining mass after pyrolysis is about 14%, which is consistent with the theoretical mass ratio of titanium dioxide in the composite material. SEBS begins to pyrolyze at 330 °C, the mass loss rate reaches the maximum at about 450 °C, and is completely pyrolyzed at about 480 °C. Both SP3 and SP4 exhibit a two-stage thermal decomposition behavior. The first stage corresponds to the pyrolysis of PW, with a temperature range of 200–350 °C; the second stage corresponds to the pyrolysis of SEBS, with a temperature range of 330–480 °C. Due to the difference in SEBS content, the residual mass ratio of SP3 after pyrolysis is slightly higher than that of SP4. This is because the addition of SEBS reduces the relative mass fraction of TiO<sub>2</sub>, and SEBS decomposes completely without residue at high temperatures. Combined with the DTG curve in Figure 3d, both pure PW and SP1 show only a single peak in the range of 300–320 °C, which corresponds to the maximum pyrolysis rate of PW. In contrast, SP3 and SP4 exhibit two symmetric characteristic peaks: the first peak, in the range of 300–320 °C, corresponds to the maximum pyrolysis rate of PW; the second peak, in the range of 440–460 °C, corresponds to the maximum pyrolysis rate of SEBS. Moreover, the intensity of the second peak of SP4 is higher than that of SP3, which is attributed to the higher SEBS content in SP4, while the peak position shows no shift. In addition, all samples show no obvious mass loss in the temperature range from room temperature to 200 °C, a phenomenon that rules out the interference of adsorbed water or low-boiling-point impurities. Furthermore, there is no characteristic decomposition peak of Ti(OH)<sub>4</sub> (the intermediate product of TiO<sub>2</sub> hydrolysis) in any of the samples, and this result confirms that TBT has been completely hydrolyzed to form stable TiO<sub>2</sub>. Both SP3 and SP4 demonstrate excellent thermal stability below 200–350 °C, and this thermal stability can meet the conventional operating temperature requirements of electronic devices and BTM systems, where the conventional operating temperature is usually below 100 °C. Although SP4 has a lower pyrolytic residual amount, its thermal stability does not deteriorate. This characteristic provides thermal safety support for SP4 to be selected as a preferred sample for BTM.

In practical applications, PCMs sometimes need to be used in high-temperature environments, so their antileakage performance is crucial for the stability and reliability of the materials. High-temperature conditions may cause the materials to soften and increase their fluidity, thereby affecting their morphological stability and service life. To explore the effect of TBT mass on the leakage rate of samples and optimize the reaction conditions, leakage rate tests were carried out. The experiments showed that PW was almost completely melted after heating for 25 min, so the leakage rate test was standardized at 25 min, with photos taken every 5 min. Finally, the final leakage temperature distribution was captured by a thermal imager. As shown in Figure 3e, with the addition of SEBS, the leakage rate of the composite material first increased slightly, from 0.50% for SP1 to 0.62% for SP2, but gradually decreased with the further increase of SEBS mass. This phenomenon is consistent with theoretical predictions. Theoretically, the more SEBS is added, the lower the mass of

titanium dioxide generated by TBT hydrolysis, and the lower the mass of the titanium dioxide skeleton coating the phase change material, so the leakage rate of the material will increase. However, SEBS has certain coating properties. With the increase of its mass, the coating of the phase change material is gradually enhanced, thereby improving the binding effect and leading to a decrease in the leakage rate.

Thermal conductivity is an important parameter for materials in thermal management applications. Thermal conductivity was measured at a temperature of 297.5 K. To ensure the reproducibility of measurements, five separate tests were conducted for each sample group. The test results are shown in Figure 3f. Nanotitanium dioxide significantly improves the thermal conductivity of the composite material. Compared with pure PW, the thermal conductivity of the SP1 sample is increased by 6.4%. In other composites, the addition of SEBS reduces the thermal conductivity of the composites, and this decreasing trend is more significant with the increase of SEBS content. However, its thermal conductivity is still slightly improved compared with PW.

For practical applications, PCMs require not only excellent thermal properties but also satisfactory mechanical properties. Figure 3g demonstrates that the prepared product has plasticity and good flexibility. The compressive strength stress-strain curve serves as a key basis for evaluating the compressive properties of materials. By applying pressure to samples under different loading conditions using an electronic universal testing machine, while collecting corresponding stress and strain data, a complete stress-strain response curve is obtained. To more distinctly highlight the mechanical properties of the material, we have retained the previous test data.<sup>[51]</sup> As shown in Figure 3h, SP1 without added SEBS, within the strain range of 0–10%, its compressive stress rises rapidly with increasing strain, reaching 1.5 MPa, indicating high stiffness. In contrast, for sample SP2 with a small amount of SEBS added, the growth rate of compressive stress is significantly slowed, with the stress only reaching 0.7 MPa at 10% strain. Samples SP3 and SP4 exhibit almost no stress, demonstrating that the addition of SEBS effectively reduces the stiffness of the material. As the load continues to increase, the material enters the elastoplastic stage, where the relationship between stress and strain is no longer linear but changes in a curved form. Part of the load causes plastic deformation of the material, accompanied by energy dissipation. The slope in this stage determines the material's plastic deformation capacity. In the strain range of 10–70%, with the continuous increase of the load, the compressive stresses of SP1 and SP2 both show a trend of slow increase, reaching 3.6 and 2.4 MPa respectively at 70% strain. However, SP3 and SP4 with higher SEBS content exhibit lower stresses, 1.0 and 0.5 MPa respectively, indicating that adding more SEBS significantly reduces the stress response of the material in the elastoplastic stage. When the load continues to rise, the material enters the plastic stage, where the stress-strain relationship becomes nonlinear, and plastic deformation gradually dominates, possibly leading to material failure or damage. The compressive strength of the material reaches its maximum value in this stage. The figure shows that in the strain range of 70–100%, the compressive stresses of SP1, SP2, and SP3

increase rapidly. The stress of SP1 reaches 16.7 MPa at 90% strain, while SP4 with the highest SEBS content shows a relatively slow stress increase, only 6.2 MPa at 90%, which is 63% lower than that of SP1. This indicates that the addition of SEBS delays the failure process of the material. Subsequently, the tensile properties of the products were tested, as shown in Figure 3i. The stress-strain curve of sample SP1 exhibits typical brittle characteristics. The curve shows a certain stress growth rate in the initial stage, but its elongation at break is only 30.73%, and the maximum tensile strength is only 3.26 MPa, with fracture occurring at 30% strain. Compared with SP1, sample SP2 with a small amount of SEBS added shows certain improvements in tensile strength and elongation at maximum force. Sample SP4 with a moderate content of SEBS exhibits a high tensile strength of 18.94 MPa in the stress-strain curve, indicating that SEBS not only enhances the flexibility of the material but also improves its overall mechanical stability, which helps to extend its service life and broaden its application range. As shown in **Table 3**, when compared with similar materials added with SEBS, the material developed in this study exhibits significant advantages in tensile properties. Meanwhile, its latent heat value remains within a favorable range, demonstrating superior comprehensive application potential.

Thermal uniformity is an important parameter for evaluating the temperature distribution uniformity of PCMs during heat storage and release, directly affecting their thermal management performance in practical applications. During the phase change process, good thermal uniformity can ensure consistent temperature changes in each region inside the material, improve heat transfer efficiency, and avoid local overheating or supercooling, thereby enhancing the stability of energy storage and release. Therefore, in this study, the thermal uniformity of composite PCMs was analyzed through infrared thermal imaging technology and temperature sensing tests to monitor their temperature distribution during heating and cooling processes.

The thermal energy storage and release performance of flexible PCMs was evaluated using a heat storage and release device. The experimental platform is shown in **Figure 4a**, which consists of a heat storage and release device, data collector, data analyzer, and high/low temperature devices. And demonstrates the dimensions, contours, and front views of the flexible PCMs used for heat storage and release, with three test points (T1, T2, and T3) installed. The heat storage and release performances of three representative shape-stabilized PCM composites, SP1, SP2, and SP4,

were tested. As shown in Figure 4b-d, the slope of the temperature curve reflects the speed of temperature rise. During the melting process, the slope of the temperature curve decreases significantly, indicating that the phase change process slows down the rate of temperature change. Due to the wide phase change temperature range of PW, its melting process starts at 28 °C. Compared with SP1 and SP2, the heating process of SP4 is significantly faster, which can raise the temperature to the melting point within 2000s, while SP1 requires 3500 s. This result shows that the uniform mixing of the flexible material SEBS and PW significantly improves the thermal response rate of the composite material. Therefore, the thermal enhancement effect of SEBS ensures that the material has strong thermal release and storage capabilities. In addition, the temperature rises and fall curves of FPCM are quite smooth and regular, which further indicates the uniform mixing efficiency of FPCM components. It can be clearly seen that SP4 has a faster temperature response speed at different temperature points, making it more suitable as the optimal material for thermal management applications.

The application of BTM has put forward higher requirements for FPCMs. Especially in humid environments, their water resistance and stability have become the key to determining the service life of the materials. The intrusion of moisture may not only cause leakage or expansion of the phase change substances inside the materials, but also reduce the thermal stability of the materials, affect their latent heat storage capacity and cyclic service life, thereby limiting their practical applications in high-humidity environments or under water contact conditions. Therefore, improving the hydrophobic performance of FPCMs is an important research direction to ensure their long-term reliability. The phase change material PW used in this work is a typical hydrophobic material, mainly composed of high-carbon chain alkanes, with low surface free energy, which enables it to effectively repel water at room temperature. In this study, the water contact angle of the flexible phase change material under different temperature conditions will be measured to analyze the influence of temperature on the surface structure and wetting behavior of the flexible phase change material. As shown in Figure 4e, a water contact angle measurement platform was constructed to evaluate the surface hydrophobic performance of the samples.

As shown in Figure 4f1, the influence of different SEBS addition amounts on the water contact angle of FPCMs under the same temperature conditions is demonstrated. It can be seen from the figure that the water contact angle of the sample without SEBS addition is 48°, and with the increase of SEBS addition, the water contact angle of the material gradually increases. When the SEBS addition reaches 1.5 g, the water contact angle rises to 78°. The research results show that the addition of SEBS effectively improves the hydrophobic performance of the flexible phase change material, making its surface more difficult to be wetted by water. In addition, the microsurface roughness of SEBS will not change significantly due to the increase of temperature, so that the droplets can still maintain a high contact angle and reduce the spreading effect of water. At higher temperatures,

**Table 3.** Comparison with materials of similar systems added with SEBS.

Literatures	Material	Latent heat of melting [J g <sup>-1</sup> ]	Tensile strength [MPa]
This work	SEBS + PW + TiO <sub>2</sub>	116.3	18.94
[53]	SEBS + PA + EG	167.4	0.23
[54]	SEBS + n-heptadecane	73	9.96
[55]	SEBS + PW + PP fiber	180.1	3.89
[56]	SEBS + PA + CF	168.11	2

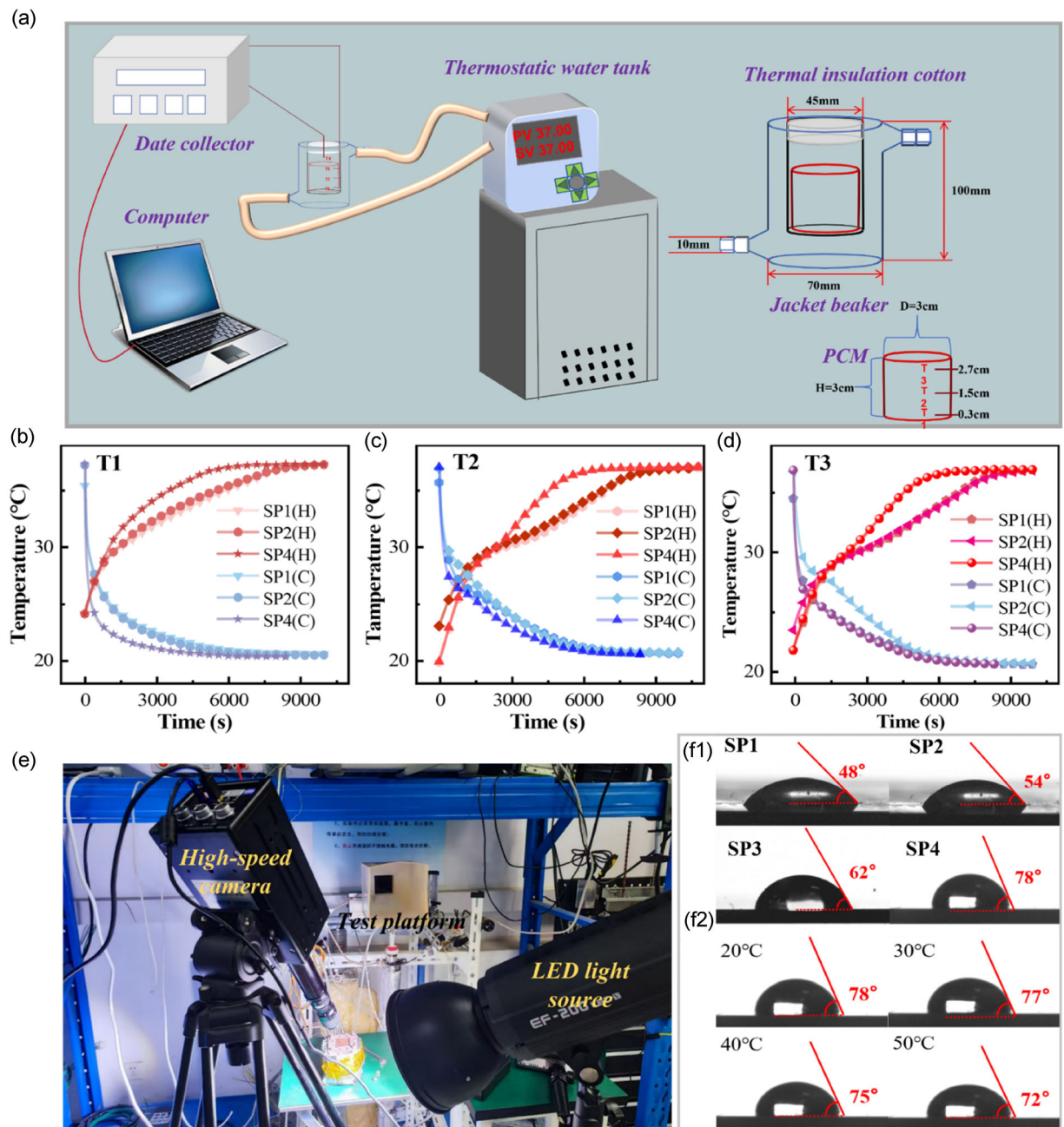


**Figure 4.** Thermal property analysis of the product. a) Thermal storage and release testing device; b) Heating and cooling curves at T1; c) Heating and cooling curves at T2; d) Heating and cooling curves at T3; e)The water contact angle analysis device; f1) Water contact angle at ambient temperature of SP1, SP2, SP3, and SP4. f2) Water contact angle of SP4 at different temperatures.

the material may soften or deform, leading to changes in the surface microstructure, which in turn affects the spreading behavior of water droplets on the surface. Compared with other PCMs or polymers, SEBS can maintain good morphological stability within a certain temperature range, avoiding the decline of hydrophobic performance caused by phase change or softening. Therefore, in the application of FPCMs, SEBS can be used as an effective hydrophobic protective layer to provide long-term stable waterproof performance for composite materials, and is suitable for BTM, smart textiles, flexible electronics and other fields. As shown in

Figure 4f2, the water contact angle of SP4 decreases with the increase of temperature, from 78° at 20 °C to 72° at 50 °C, a decrease of 7.7%. Compared with SP1, the decrease in the water contact angle of SP4 is smaller. Its hydrophobic performance is less affected by temperature. Especially at 50 °C, SEBS can still maintain relatively stable hydrophobic properties. When the temperature rises to 50 °C, the mobility of SEBS molecular chains increases to some extent, but the overall structure remains complete, and the surface morphology does not change significantly. Therefore, the water contact angle does not change much,

showing stable hydrophobic performance. In addition, the microscopic surface roughness of SEBS will not change significantly due to the increase of temperature, so that the droplets can still maintain a high contact angle and reduce the spreading effect of water. At higher temperatures, the material may soften or deform, leading to changes in the surface microstructure, which in turn affects the spreading behavior of water droplets on the surface. Compared with other PCMs or polymers, SEBS can maintain good morphological stability within a certain temperature range, avoiding the decline of hydrophobic performance caused by phase change or softening. Therefore, in the application of FPCMs, SEBS can be used as an effective hydrophobic protective layer to provide long-term stable waterproof performance for composite materials, which is suitable for BTM.

### 3.3. Application

FPCMs with their excellent heat storage and release capabilities, good mechanical flexibility, and customizability, provide an efficient temperature control strategy for BTM. This experiment focuses on the application of FPCMs in BTM, systematically evaluates their effect on battery temperature regulation, discusses the compatibility between PCMs and battery structures, and verifies their impact on battery life and safety through cyclic tests, providing experimental evidence for the application of FPCMs in advanced energy storage systems. Figure 5a shows the experimental setup of BTM system.

As shown in Figure 5b, a foam box and thermal insulation cotton were used to construct adiabatic conditions for the battery. Thermocouples were attached to the two poles and the middle of the battery to monitor temperature changes. The charging and discharging steps were cycled multiple times, and the battery temperature changes over time were measured and recorded. In the blank group, only thermal insulation cotton and a foam box were used. In the experimental group, 500 g of FPCM was made into a hollow cylinder for placing the battery. After inserting the battery, 100 g of PCM was used to seal the two poles, and then thermal insulation cotton was covered on the surface of the FPCM. The lithium iron phosphate battery employed in this study is a prismatic cell commonly used in energy storage systems, with a nominal capacity of 10 Ah and a nominal voltage of 3.2 V. It operates within a temperature range of -20 °C to 60 °C, and 70 °C is set as the critical safety threshold in this research. The electrodes consist of a graphite anode, a lithium iron phosphate cathode, and an organic electrolyte, with dimensions of 100 × 70 × 10 mm, which are consistent with the encapsulation size of the phase change material described in Figure 5b. When selecting BTM materials, conductive fillers or structures should be avoided as much as possible to reduce the risk of battery short circuits, extend service life, and ensure the normal operation of the battery management system. In addition, conductive materials may accelerate the degradation of the electrolyte, affecting the overall performance and stability of the battery. Therefore, in the material selection process, while ensuring good thermal management performance, electrical insulation should be

prioritized to improve the safety and reliability of the battery system. To ensure the safety of the test, the conductivity of the material was tested, and the results showed that the material had infinite resistance and no conductivity.

SP4 was selected as the sample for application experiments due to its comprehensive performance that best fits the requirements of BTM. It contains the highest proportion of SEBS, with a 200% increase in elongation at break and a tensile strength of 18.94 MPa, thus combining high flexibility and structural stability, which allows it to fit the irregular surfaces of battery modules and withstand vibration and extrusion. Thermal storage and release tests show that its time to reach the melting point is much shorter than that of other samples, enabling it to quickly absorb pulsed heat generated during high-rate charge-discharge processes. Additionally, its smooth temperature curve ensures uniform heat distribution. The leakage rate of SP4 is lower after optimization by SEBS, with a water contact angle of 78° and only a 7.7% decrease in hydrophobic performance at 50 °C, making it suitable for humid environments. Meanwhile, it possesses electrical insulation, balancing heat dissipation efficiency and battery safety. As shown in Figure 5c, the measurement results indicate that during the charging and discharging process of the lithium iron phosphate battery, the temperature in the middle region is higher than that at the two poles. This is mainly due to the uneven distribution of internal resistance, where the ohmic impedance and polarization impedance in the central region are relatively large, leading to easier heat accumulation. In addition, the heat dissipation efficiency of the battery tabs and casing is relatively high, resulting in lower temperatures at the two poles. Meanwhile, the electrochemical reactions inside the battery are not uniformly distributed, and the active materials in the central region release more heat, exacerbating the temperature difference. The limited thermal conduction path also hinders the heat transfer from the middle to the outside, further increasing the temperature in the central region. Generally, the internal temperature of the battery is 5–10 °C higher than the surface temperature. Since the maximum operating temperature of the battery used in this experiment is 80 °C, the surface temperature of 70 °C is set as the dangerous temperature. When the surface temperature rises to 70 °C, the charging and discharging process is immediately stopped, while 20–50 °C is defined as the normal operating temperature.

At a 2C charging and discharging rate, the middle temperature of the battery in the blank group took 0.3 h to rise from the initial temperature of 20 °C to about 50 °C, and a cumulative 1.3 h to continue rising to about 70 °C. At a 3C charging and discharging rate, the middle temperature of the battery in the blank group took 0.2 h to rise from 20 °C to about 50 °C, and a cumulative 0.6 h to rise to about 70 °C. For these two groups of charging and discharging rates, BTM is required to ensure the stability and safety of battery operation. When charging and discharging the battery at a 1C rate, it took 8 h for the middle temperature of the battery to rise to about 50 °C. Although temperatures exceeding 50 °C do not cause significant immediate impacts on the battery, prolonged operation above 50 °C will lead to significant battery capacity degradation and shortened driving range. Therefore,

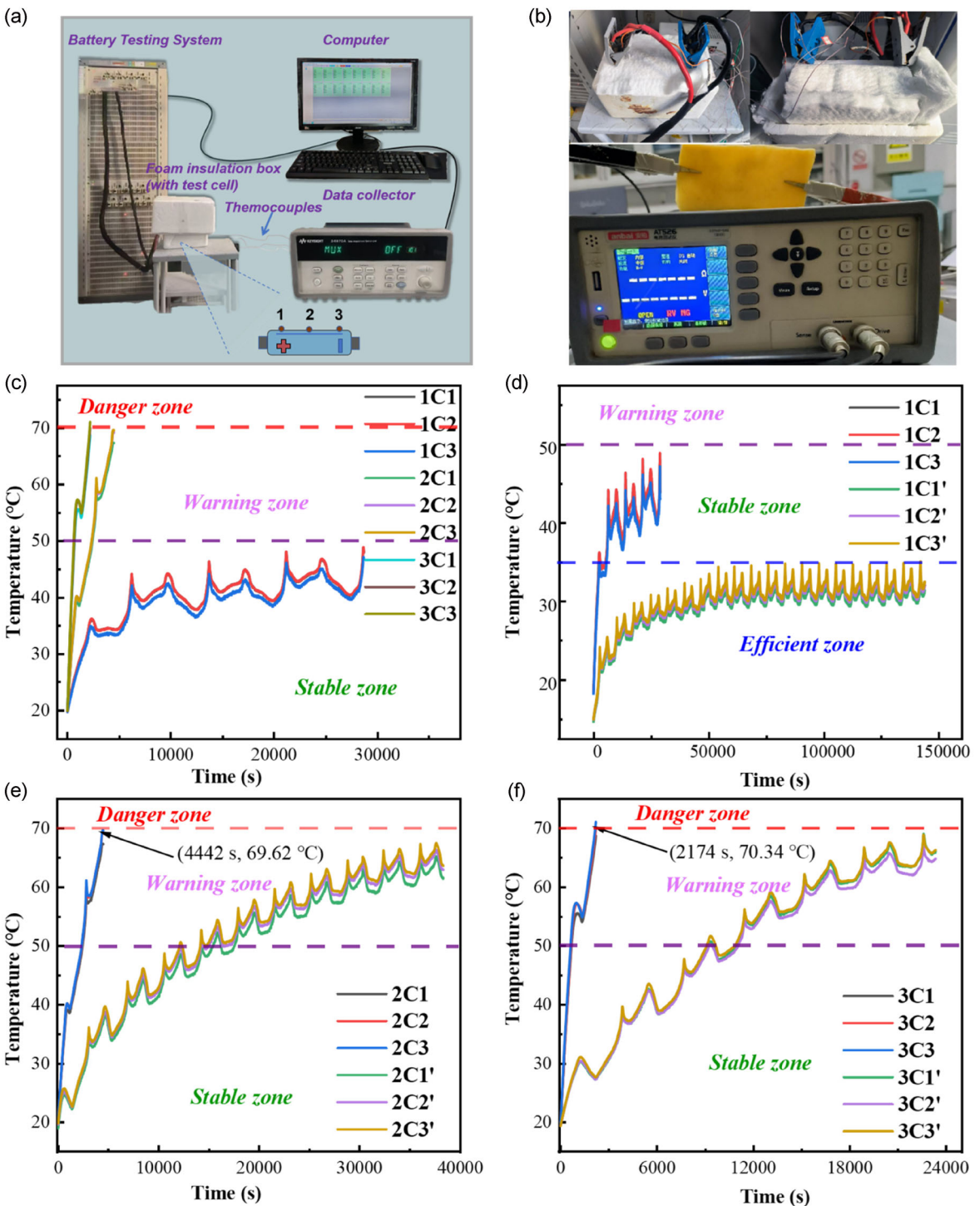


**Figure 5.** Application of BTM. a) BTM testing device; b) BTM testing environment; c) Comparison of the blank group under different charge and discharge rates; d) Comparison of temperature control performance at 1C charge and discharge rate; e) Comparison of temperature control performance at 2C charge and discharge rate; and f) Comparison of temperature control performance at 3C charge and discharge rate.

under the condition of 1C charging and discharging rate, it is necessary to maintain the battery temperature below 50 °C as much as possible to avoid reaching the critical operating temperature.

As shown in Figure 5d, under the charge-discharge condition at 1C rate, since the temperature change was insignificant in the subsequent long period, only partial temperature change data

are presented. The battery temperature in the experimental group remained below 35 °C for nearly 40 h, while the blank group reached 35 °C in only 0.6 h. When the experimental group operated under 1C charge-discharge conditions for 0.6 h, the battery temperature was only 20.4 °C, and the middle temperature of the battery decreased by 41.7% compared with the same

operation time. The use of FPCMs significantly prolonged the time for the battery to maintain temperature efficiently. In the adiabatic environment, the surface temperature of the lithium iron phosphate battery did not rise for a long time, mainly because a short-term thermal balance was formed between the heat absorption capacity of PCM and the heat generation rate of the battery, that is, the phase change latent heat absorption process inhibited the temperature rise. The phase change temperature of the used phase change material was exactly around 32 °C. PCMS absorbs the heat released by the battery through the latent heat of phase change, so that the temperature remains stable near the phase change temperature. At the same time, its low thermal conductivity limits the outward diffusion of heat and slows down the temperature rise rate. When the heat absorbed by PCMS matches the heat released by the battery, the system enters a short-term dynamic balance, resulting in no obvious change in surface temperature. Since the heat generation of the battery is not very large under the charge-discharge condition at 1C rate, PCMS will not gradually reach thermal saturation, so the battery continues to generate heat, but the temperature does not continue to rise.

As can be seen from Figure 5e, under the charge-discharge condition at 2C rate, the experimental group took 3.4 h to rise from the initial temperature of 20 °C to about 50 °C, and continued to rise to about 70 °C for a cumulative 10.5 h, which increased by 1033% and 708% respectively compared with the temperature maintenance time of the blank group. After the 2C charge-discharge program was executed for 0.3 h, the middle temperature of the battery in the blank group rose to 50 °C, and the temperature of the experimental group was only 28.6 °C. The middle temperature of the battery decreased by 42.8% under the same operation time. When the charge-discharge program continued to 1.3 h, the middle temperature of the battery in the blank group further rose to 70 °C, while the temperature of the experimental group remained at 38.7 °C, with a decrease of 44.7%. In addition, during the 10.5 h test process, the temperature of the battery in the experimental group was completely kept within the normal and critical operating temperature ranges, accounting for 32.4% and 67.6% of the time respectively.

It can be seen from Figure 5f that under the charge-discharge condition at 3C rate, the battery temperature of the experimental group took 2.5 h to rise from the initial temperature of 20 °C to about 50 °C, and continued to rise to about 70 °C for a cumulative 6.3 h. Compared with the blank group, the experimental group showed significant advantages in temperature maintenance time, which were increased by 1150% and 950%, respectively. Further analysis of the experimental results under the 2C rate

charge-discharge conditions showed that after the charge-discharge program was run for 0.2 h, the middle temperature of the battery in the blank group quickly rose to 50 °C, while the temperature of the experimental group was only 26.6 °C, and the middle temperature of the battery decreased by 46.8% in the same running time. When the charge-discharge program continued to 0.6 h, the middle temperature of the battery in the blank group further rose to 70 °C, while the temperature of the experimental group remained stable at 27.7 °C, with a decrease of 60.4%. This result further verifies the excellent performance of the experimental group in high-temperature environments. In addition, during the 6.3 h test process, the temperature of the battery in the experimental group always remained within the normal operating temperature and critical operating temperature ranges. Specifically, the battery temperature was within the normal operating temperature range for 39.7% of the time and within the critical operating temperature range for 60.3% of the time.

The data show that the experimental group not only showed excellent thermal stability in high-temperature environments, but also effectively controlled the temperature throughout the test process to prevent the battery from entering a dangerous operating state. To sum up, the thermal management performance of the experimental group in high-temperature environments is significantly better than that of the blank group, which can effectively extend the operating time of the battery under high-temperature conditions and greatly reduce the middle temperature of the battery, providing a reliable guarantee for the safe operation of the battery. As shown in the comparison in Table 4, existing PCM technology routes often involve irreconcilable "performance trade-offs." Pursuing extreme thermal conductivity comes at the cost of flexibility and manufacturing costs; prioritizing low cost and flexibility sacrifices long-term packaging stability and thermal storage performance; and achieving perfect packaging performance and flexibility through methods like chemical grafting involves compromises in manufacturing costs, process complexity, and latent heat density. The OPOS-FPCM proposed in this study successfully achieves a highly competitive balance among these mutually constraining performance metrics. Through a relatively straightforward manufacturing method, it achieves the synergistic integration of high flexibility, excellent leak-proof performance, high thermal storage capacity, and good mechanical strength. Although its thermal conductivity has not yet reached the level of graphene aerogel, its balanced overall performance, particularly its ability to perfectly combine the previously conflicting characteristics of "leakage prevention" and "flexibility," makes it more promising than existing

**Table 4.** Comparison of comprehensive performance with advanced PCM technology.

Technology type	Manufacturing ease	Flexibility	Leakage resistance	Thermal storage	Cost/scalability
This study(OPOS-PCM)	Moderate	Excellent	Excellent	High	Moderate
Rigid porous scaffold PCM <sup>[57]</sup>	Complex	Poor	Excellent	Good	High
Flexible physical blending PCM <sup>[58]</sup>	Simple	Good	Poor/Average	Average	Low
Chemically grafted flexible PCM <sup>[59]</sup>	Complex	Good	Excellent	Medium	High

single-technology approaches in numerous emerging fields requiring flexibility, reliability, and efficient thermal management, such as smartwatches, fitness trackers, and flexible displays. Its flexibility and low leakage risk enable it to conform to curved surfaces, maintaining the device temperature within the range of 30–40 °C to avoid skin discomfort or performance degradation. It is suitable for flexible energy storage devices, such as foldable batteries and thin-film energy storage modules, and its mechanical toughness and stable cyclic performance ensure long-term reliability under dynamic deformation. It can be applied to electric vehicle battery packs, for instance, 48 V auxiliary batteries and 12 V starter batteries, which can significantly extend the time it takes for the battery to reach 50 °C and meet the requirements of space constraints and vibration resistance. Additionally, it is suitable for portable power stations, and its zero-power cooling mechanism can meet the passive thermal management needs of small energy storage systems for outdoor activities or emergency backup, reducing energy consumption and maintaining battery efficiency.

## 4. Conclusion

In this study, an OPOS was devised to fabricate FPCMs with in situ formed porous  $\text{TiO}_2$ , explicitly addressing thermal management challenges in electronic devices. The one-pot synthesis integrates molten PW with SEBS and TBT to form a porous  $\text{TiO}_2$  skeleton, enabling dual functions of thermal energy storage and efficient heat dissipation. The composite features a high specific surface area of 316.307  $\text{m}^2 \text{g}^{-1}$  for porous  $\text{TiO}_2$  and a leakage rate  $< 0.5\%$ , maintaining stability over 2000 thermal cycles. In thermal management applications, particularly for lithium-ion batteries, the FPCM significantly extends the time for battery temperature to rise from 20 °C to dangerous thresholds (50–70 °C) by 1033–1150% under 2–3C charge-discharge rates, while reducing the mid-battery temperature by 41.7–60.4% compared to control groups. Its electrical insulation (infinite resistance) and hydrophobicity (water contact angle up to 78°) further ensure safety and reliability in harsh environments. This work demonstrates that the FPCM combines the structural stability of porous  $\text{TiO}_2$  and the mechanical flexibility of SEBS, offering a promising solution for efficient thermal management in wearable electronics, flexible devices, and high-power energy storage systems.

The future expansion directions of this study lay a foundation for in-depth exploration of the current research and can be carried out in the following aspects: in terms of thermal conductivity optimization, although the porous  $\text{TiO}_2$  framework improves structural stability, its thermal conductivity is slightly higher than that of pure paraffin, which still has limitations; future research can introduce high thermal conductivity nanomaterials such as boron nitride nanosheets and carbon nanotubes into the  $\text{TiO}_2$ /SEBS network to construct multiscale heat conduction paths, which is expected to significantly improve thermal conductivity without sacrificing flexibility; in terms of integration with active thermal management, combining FPCMs with lightweight liquid cooling systems such as microchannel structures can build a

hybrid heat dissipation system, which uses the latent heat storage of PCMs to buffer pulse heat and dissipates accumulated heat through liquid cooling, thereby improving performance in ultrahigh-power scenarios such as battery charging at a rate of 5C and above; in terms of large-scale manufacturing, the one-pot one-step method has the potential for large-scale production, but optimizing solvent recovery such as the recycling of 1,2-dichloroethane and reducing the amount of TBT can reduce production costs, and the feasibility of large-scale production can be verified through pilot tests of the roll-to-roll process; these expansion directions will enhance the practical application value of FPCMs and fill the gaps in the field of thermal management for emerging flexible electronics and high-power electronic systems.

## Acknowledgments

This work was supported by the Fundamental Research Funds for the Central Universities (no. 2023ZDPY12). The authors also thank Dr. Hua Wei and Dr. Rui Zhou at Advanced Analysis & Computation Center of CUMT for their assistance with chemical analysis.

## Conflict of Interest

The authors declare no conflict of interest.

## Author Contributions

**Guangyuan Liang:** data curation (equal); writing—original draft (equal). **Runyang Wang:** data curation (equal); writing—original draft (equal). **Qiang Zhou:** data curation (equal). **Jiahuan He:** data curation (equal). **Yuanzheng Liu:** data curation (equal). **Jiateng Zhao:** methodology (lead). **Changhui Liu:** writing—review & editing (lead). **Guangyuan Liang** and **Runyang Wang** have been treated as co-first authors.

## Data Availability Statement

The data that support the findings of this study are available from the corresponding author upon reasonable request.

**Keywords:** battery thermal management · flexible phase change materials · porous  $\text{TiO}_2$  · thermal stability

- [1] J. Li, Y. Fu, J. Zhou, K. Yao, X. Ma, S. Gao, Z. Wang, J. G. Dai, D. Lei, X. Yu, *Sci. Adv.* **2023**, *9*, eadg1837.
- [2] Y. Cui, Z. Qin, H. Wu, M. Li, Y. Hu, *Nat. Commun.* **2021**, *12*, 1284.
- [3] P. Ball, *Nature* **2012**, *492*, 174.
- [4] T. T. Du, Z. X. Xiong, L. Delgado, W. Z. Liao, J. Peoples, R. Kantharaj, P. R. Chowdhury, A. Marconnet, *Nat. Commun.* **2021**, *12*, 4915.
- [5] Q. Cai, D. Scullion, W. Gan, A. Falin, S. Zhang, K. Watanabe, T. Taniguchi, Y. Chen, E. J. G. Santos, L. H. Li, *Sci. Adv.* **2019**, *5*, eaav0129.
- [6] A. H. Khalaj, S. K. Halgamuge, *Appl. Energy* **2017**, *205*, 1165.
- [7] F. S. Hwang, T. Confrey, C. Reidy, D. Picovici, D. Callaghan, D. Culliton, C. Nolan, *Renewable Sustainable Energy Rev.* **2024**, *192*, 114171.
- [8] Y. Zhao, X. Zhang, B. Yang, S. Cai, J. *Energy Storage* **2024**, *76*, 109836.

- [9] W. Wang, K. Wang, P. Li, M. Wang, *Chem. Eng. J.* **2023**, *471*, 144555.
- [10] C. Wang, L. Hua, H. Yan, B. Li, Y. Tu, R. Wang, *Joule* **2020**, *4*, 435.
- [11] C. Zhang, Y. Mao, K. Li, Y. Liu, Z. Xu, K. Pang, S. Cai, L. Fan, C. Gao, *Energy Storage Mater.* **2025**, *75*, 104003.
- [12] Q. Wang, J. Wang, K. Ma, Q. Mao, Y. Shi, *J. Energy Storage* **2024**, *97*, 112971.
- [13] R. Luo, L. Wang, W. Yu, F. Shao, H. Shen, H. Xie, *Appl. Energy* **2023**, *331*, 120377.
- [14] J. Li, W. Duan, Y. Chen, H. Chen, M. Song, S. Liao, E. Shi, X. Sun, *Appl. Therm. Eng.* **2024**, *250*, 123456.
- [15] Z. Zhao, X. Feng, D. Feng, C. Li, Y. Feng, J. Wei, *Front. Energy* **2025**, *19*, 227.
- [16] X. Dai, P. Ping, D. Kong, X. Gao, Y. Zhang, G. Wang, *J. Energy Chem.* **2024**, *89*, 226.
- [17] J. Lin, D. Liu, X. Liu, M. Liu, Y. Cui, *Appl. Therm. Eng.* **2025**, *262*, 125240.
- [18] J. Zhang, Y. Xu, X. Li, H. Li, C. Yao, S. Chen, F. Xu, *Energy Convers. Manage.* **2022**, *256*, 115357.
- [19] H. Zhu, M. Gu, X. Dai, S. Feng, T. Yang, Y. Fan, J. Zhang, D. Fan, Y. Liu, Y. Lu, P. Zhu, H. Lu, T. Qian, Y. Cao, C. Yan, *Chem. Eng. J.* **2024**, *494*, 153235.
- [20] X. W. Lin, Q. D. Wang, X. G. Zhu, M. Y. Shi, Z. F. Zhou, *J. Mol. Liq.* **2024**, *404*, 124993.
- [21] C. Liu, T. Xiao, J. Zhao, Q. Liu, W. Sun, C. Guo, H. M. Ali, X. Chen, Z. Rao, Y. Gu, *Renewable Sustainable Energy Rev.* **2023**, *188*, 113814.
- [22] Y. Li, X. Huang, X. Huang, X. Gao, R. Hu, X. Yang, Y. L. He, *Appl. Energy* **2023**, *347*, 121458.
- [23] S. Wang, K. Lei, Z. Wang, H. Wang, D. Zou, *Chem. Eng. J.* **2022**, *438*, 135559.
- [24] G. Zhu, M. Zou, W. Luo, Y. Huang, W. Chen, X. Hu, X. Jiang, Q. Li, *Chem. Eng. J.* **2024**, *488*, 150930.
- [25] C. Liang, W. Zhang, C. Liu, J. He, Y. Xiang, M. Han, Z. Tong, Y. Liu, *Chem. Eng. J.* **2023**, *471*, 144500.
- [26] G. Liang, X. Zhang, J. Zhao, L. Geng, Y. Lin, Y. Liu, J. Gao, C. Liu, *Small* **2025**, *21*, 2503431.
- [27] Y. Cao, G. Li, J. He, L. Geng, G. Liang, X. Du, Y. Liu, C. Liu, *J. Energy Storage* **2025**, *125*, 17052.
- [28] S. Zhang, Z. Li, Y. Yao, L. Tian, Y. Yan, *Nano Energy* **2022**, *100*, 107476.
- [29] Z. Tang, H. Gao, X. Chen, Y. Zhang, A. Li, G. Wang, *Nano Energy* **2021**, *80*, 105454.
- [30] X. Lu, R. Qian, X. Xu, M. Liu, Y. Liu, D. Zou, *Nano Energy* **2024**, *124*, 109520.
- [31] R. Ehid, A. S. Fleischer, *Energy Convers. Manage.* **2012**, *53*, 84.
- [32] C. Liu, J. Zhang, J. Liu, Z. Tan, Y. Cao, X. Li, Z. Rao, *Angew. Chem. Int. Ed.* **2021**, *60*, 13978.
- [33] Z. Wang, S. Liu, C. Zhu, J. Xu, *Adv. Mater.* **2024**, *36*, 2403889.
- [34] H. Y. Guo, W. C. Jiao, H. Z. Jin, Z. J. Yuan, X. D. He, *Adv. Funct. Mater.* **2023**, *33*, 2209345.
- [35] Y. Lin, Q. Kang, Y. Liu, Y. Zhu, P. Jiang, Y. W. Mai, X. Huang, *Nano-Micro Lett.* **2023**, *15*, 31.
- [36] K. Xu, G. Zhang, Y. Li, Y. Feng, X. Yin, *J. Energy Storage* **2024**, *98*, 113190.
- [37] Y. C. Zhou, J. Yang, L. Bai, R. Y. Bao, M. B. Yang, W. Yang, *J. Mater. Chem. A.* **2022**, *11*, 341.
- [38] J. Shi, M. Qin, W. Aftab, R. Zou, *Energy Storage Mater.* **2021**, *41*, 321.
- [39] Y. Li, M. Wang, G. Zhang, X. Chen, Y. He, X. Zhi, Q. Zhao, X. Sun, C. Huang, *Int. J. Hydrogen Energy* **2024**, *58*, 93.
- [40] Z. Tao, X. Chen, M. Yang, X. Xu, Y. Sun, Y. Li, J. Wang, G. Wang, *Sol. Energy Mater. Sol. Cells* **2020**, *215*, 110600.
- [41] R. Chen, X. Huang, W. Deng, R. Zheng, W. Aftab, J. Shi, D. Xie, R. Zou, Y. Mei, *Appl. Energy* **2020**, *260*, 114320.
- [42] Y. Kou, K. Sun, J. Luo, F. Zhou, H. Huang, Z. S. Wu, Q. Shi, *Energy Storage Mater.* **2021**, *34*, 508.
- [43] Y. Jing, Z. Zhao, X. Cao, Q. Sun, Y. Yuan, T. Li, *Nat. Commun.* **2023**, *14*, 8060.
- [44] H. Nazir, M. Batool, M. Ali, A. M. Kannan, *Appl. Therm. Eng.* **2018**, *142*, 466.
- [45] C. Hong, J. Ren, X. Kong, *Appl. Therm. Eng.* **2024**, *243*, 122599.
- [46] B. Hu, J. Li, X. Du, Z. Zhang, H. Wang, *J. Energy Storage* **2024**, *99*, 113349.
- [47] T. Luo, L. Kong, J. Lu, M. Xie, B. Lin, L. Fu, B. Huang, C. Xu, *Adv. Mater.* **2024**, *36*, 2411820.
- [48] Q. Q. Deng, Y. B. Tao, X. K. Yu, S. Q. Wang, H. Ye, *Sol. Energy Mater. Sol. Cells* **2024**, *273*, 112929.
- [49] T. Luo, L. Kong, L. Li, J. Lu, Z. Yu, B. Lin, L. Fu, C. Xu, *Chem. Eng. J.* **2024**, *486*, 150443.
- [50] A. R. Muchtar, C. L. Hassam, B. Srinivasan, D. Berthebaud, T. Mori, N. Soelami, B. Yuliarto, *J. Energy Storage* **2022**, *52*, 104974.
- [51] R. Wang, L. Geng, X. Zhang, G. Liang, J. Zhao, C. Liu, *Chem. Eng. J.* **2025**, *505*, 159592.
- [52] Q. Liu, T. Xiao, J. Zhao, W. Sun, C. Liu, *Small* **2023**, *19*, 2204998.
- [53] J. Yuan, Y. Yan, X. Kong, C. Wang, M. Fan, *Compos. Struct.* **2025**, *353*, 118718.
- [54] Y. Zhao, S. Shen, X. Wang, R. Cao, X. Jia, X. Niu, H. Liu, X. Zhang, *Energy Build.* **2023**, *285*, 112933.
- [55] X. Kong, Y. Fu, J. Yuan, *Appl. Energy* **2023**, *348*, 121556.
- [56] C. Hu, Y. Jiang, S. Chen, L. Wang, H. Li, Y. Li, D. Tang, *J. Energy Storage* **2023**, *73*, 108918.
- [57] M. S. Isfahani, A. Gharehghani, S. Saeedipour, M. Rabiei, *J. Energy Storage* **2023**, *72*, 108789.
- [58] R. Dai, G. Li, L. Xiao, Y. Li, Z. Cui, L. Jia, M. Zhou, Y. Song, Y. Yang, Y. Cai, C. Chen, K. Yin, *Chem. Eng. J.* **2022**, *446*, 136874.
- [59] F. Wei, C. P. Feng, J. Yang, L. Y. Yang, L. Bai, R. Y. Bao, Z. Y. Liu, M. B. Yang, W. Yang, *ACS Appl. Mater. Interfaces* **2021**, *13*, 59364.

Manuscript received: June 17, 2025

Revised manuscript received: September 1, 2025

Version of record online: